

Quantum-classical Liouville dynamics of nonadiabatic proton transfer

Gabriel Hanna^{a)} and Raymond Kapral

Chemical Physics Theory Group, Department of Chemistry, University of Toronto, Toronto, Ontario M5S 3H6, Canada

(Received 30 March 2005; accepted 29 April 2005; published online 30 June 2005)

A proton transfer reaction in a linear hydrogen-bonded complex dissolved in a polar solvent is studied using mixed quantum-classical Liouville dynamics. In this system, the proton is treated quantum mechanically and the remainder of the degrees of freedom is treated classically. The rates and mechanisms of the reaction are investigated using both adiabatic and nonadiabatic molecular dynamics. We use a nonadiabatic dynamics algorithm which allows the system to evolve on single adiabatic surfaces and on coherently coupled pairs of adiabatic surfaces. Reactive-flux correlation function expressions are used to compute the rate coefficients and the role of the dynamics on the coherently coupled surfaces is elucidated. © 2005 American Institute of Physics.

[DOI: 10.1063/1.1940051]

I. INTRODUCTION

Proton transfers comprise an important class of reactions that play a significant role in many chemical and biological processes.¹ In order to be able to determine the mechanisms and compute the rates of such reactions, one must account for the way the solvent or other environmental degrees of freedom participate in the proton transfer reaction. In addition, since the proton is a light particle, its quantum-mechanical character cannot be neglected.

Proton transfers in the condensed phase or biochemical systems take place in complex many-body environments with a very large number of degrees of freedom. It is not possible to simulate the quantum-mechanical equations of motion for such large systems to obtain the reaction rate. Since the dynamics of the relatively heavy molecules comprising the environment or bath can often be approximated by classical mechanics, mixed quantum-classical methods that combine a quantum-mechanical treatment of the proton while retaining a classical description of the bath provide a means to study proton transfer processes.^{2–5}

One of the simplest of such mixed quantum-classical schemes is adiabatic dynamics where the Born–Oppenheimer approximation is invoked to solve the Schrödinger equation for the protonic degrees of freedom for a fixed set of bath coordinates. The ground-state energy of the proton then serves as the potential energy to evolve the classical degrees of freedom by Newton's equations of motion.⁶

Adiabatic dynamics does not allow for the possibility that the Born–Oppenheimer approximation may break down as a result of coupling between the protonic and bath degrees of freedom. Such breakdown will lead to nonadiabatic transitions among the adiabatic states, which will modify the

mechanism and rate of the reaction. Surface-hopping methods have been constructed to account for such nonadiabatic effects.^{7–9}

In this article we use quantum-classical Liouville dynamics to determine the mechanism and compute the rate of a model condensed phase proton transfer process. The focus of the article is primarily on the techniques needed to solve this problem. The model system is specified in Sec. II. Section III on adiabatic dynamics describes the appropriate choice of reaction coordinate for the proton transfer and outlines the rare event sampling scheme used to compute the rate constant. The main results of the study are presented in Sec. IV. Expressions for the nonadiabatic rate constant are given along with the method used to simulate the quantum-classical Liouville evolution needed to evaluate the rate constant. Some aspects of the results are discussed in the Conclusions.

II. MODEL

We consider a model for a proton transfer reaction ($AH-B \rightleftharpoons A^- - H^+B$) in a linear hydrogen-bonded complex (AHB) dissolved in a polar solvent which was constructed by Azzouz and Borgis¹⁰ and later investigated by several groups using a wide variety of approaches.^{11–16} The specific forms of the interaction potentials used in this study can be found in Ref. 11. Since the complex is linear, the position of the proton is described by a one-dimensional coordinate operator \hat{q} , which measures the distance between the center of mass of the complex and the proton.

The potential-energy function describing the gas-phase hydrogen bonding interaction within the complex was chosen to model a slightly strongly hydrogen-bonded phenol (A) trimethylamine (B) complex. The masses of A and B were taken as those of phenol ($m_A=93$ amu) and trimethylamine ($m_B=59$ amu), respectively. The parameters which control the strength of the $A-B$ bond were chosen to yield an equi-

^{a)}Electronic mail: ghanna@cptg.chem.utoronto.ca

librium $A-B$ separation of $R_{AB}=2.7$ Å. For this value of R_{AB} , the potential-energy function has two minima, the deeper minimum corresponding to the stable covalent state ($q=0.048$ Å) and the shallower minimum corresponding to the metastable ionic state ($q=-0.552$ Å). In the calculations presented in this paper we have constrained R_{AB} to be 2.7 Å. Although we have constrained the R_{AB} distance to illustrate the methodology in a simpler context, we note that vibration of the complex influences the proton transfer process. This more general situation may also be treated using the techniques developed in this paper.

An important feature of this model is the variation of the charge distribution in the AHB complex, which results from the motion of the proton along the $A-B$ axis. To achieve this, a set of coordinate-dependent point charges is assigned to A , H , and B . The covalent state of the complex has a molecular dipole moment of $\mu=2.5$ D, and that of the ionic state is $\mu=10.5$ D

The AHB complex is dissolved in a solvent composed of 255 polar, nonpolarizable model methyl chloride molecules. The methyl group is approximated by a single atomic site, and the distance between the methyl and chloride groups is constrained to be 1.781 Å using the SHAKE algorithm.¹⁷

The time evolution of the system is studied using mixed quantum-classical Liouville dynamics which involves the Hamiltonian operator partially Wigner transformed¹⁸ over the solvent and A and B groups of the complex. It is given by

$$\begin{aligned}\hat{H}(\hat{q}, R) &= K_S + K_C + \hat{K}_P + V_{SS}(R) + \hat{V}_{CS}(\hat{q}, R) \\ &\quad + \hat{V}_{PS}(\hat{q}, R) + \hat{V}_{PC}(\hat{q}, R_{AB}) \\ &= K_S + K_C + \hat{K}_P + \hat{V}(\hat{q}, R), \\ &= K_S + K_C + \hat{H}_P(\hat{q}, R),\end{aligned}\quad (1)$$

where $\hat{V}(\hat{q}, R) = V_{SS}(R) + \hat{V}_{CS}(\hat{q}, R) + \hat{V}_{PS}(\hat{q}, R) + \hat{V}_{PC}(\hat{q}, R_{AB})$ is the total potential-energy operator, and $\hat{H}_P(\hat{q}, R) = \hat{K}_P + \hat{V}(\hat{q}, R)$ is the protonic Hamiltonian. The protonic kinetic-energy operator is $\hat{K}_P = \hat{p}^2/2m_p$, where m_p is the mass of the proton, and \hat{p} is the protonic momentum operator, while K_S and K_C denote the classical kinetic-energy contributions from the solvent and complex groups, respectively. The set of coordinates belonging to the classical particles is denoted by R . The quantum subsystem has position operator \hat{q} .

The solvent-solvent interactions are governed by intermolecular site-site Coulombic and Lennard-Jones (LJ) potentials. The complex-solvent interactions are governed by a site-site Lennard-Jones potential and a site-site Coulombic potential, which takes the charge variation on A and B into account. The LJ potentials were spherically truncated at $R_c = 13.8$ Å and shifted accordingly. The Coulombic potentials were smoothly truncated to zero at $R_c = 13.8$ Å. All simulations were performed at approximately 250 K in a cube with sides of length 28 Å, yielding a density $\rho = 0.012$ Å⁻³. Periodic boundary conditions were used.

III. ADIABATIC DYNAMICS

Before discussing the nonadiabatic dynamics of the proton transfer process, the main topic of this paper, we present results for adiabatic proton transfer. The adiabatic evolution of the system was carried out by solving the Schrödinger equation for the proton for fixed values of the classical bath coordinates. The ground-state adiabatic energy serves as the potential energy for the evolution of the classical phase-space variables using Newton's equations of motion; thus, the classical evolution takes place on a single adiabatic potential-energy hypersurface. These calculations allow us to construct an appropriate reaction coordinate for the proton transfer and gauge the importance of nonadiabatic surface-hopping effects.

A. Solution of the Schrödinger equation

The Schrödinger equation for the proton for a given configuration R of the classical particles is

$$\hat{H}_P(\hat{q}, R)|\alpha; R\rangle = E_\alpha(R)|\alpha; R\rangle. \quad (2)$$

In order to solve Eq. (2), the wave function $|\alpha; R\rangle$ was expanded in a set of normalized basis functions

$$|\alpha; R\rangle = \sum_i c_{i\alpha}(R)|\phi_i\rangle, \quad (3)$$

which were chosen to be the solutions of the quantum harmonic oscillator,

$$\begin{aligned}\phi_i(q) &= \langle q|\phi_i\rangle = (2^m m! \sqrt{\pi})^{-1/2} b^{1/2} H_m(b(q - q_0)) \\ &\quad \times \exp[-b^2(q - q_0)^2/2],\end{aligned}\quad (4)$$

where m is an integer, $H_m(x)$ is a Hermite polynomial, and the index i on the basis function represents a pair of values for m and q_0 . We have used a total of 12 basis functions, consisting of two sets of six functions ($m=0-5$). One set was centered at $q_0=0.048$ Å, and the other set at $q_0=-0.552$ Å, the minima of each well in the gas-phase potential. All functions had $b=7.732$ Å⁻¹, which corresponds to a proton frequency of $\omega=2000$ cm⁻¹. If we substitute the expansion in Eq. (3) into Eq. (2), we get the standard eigenvalue problem, $Hc = ScE$, where H is the Hamiltonian matrix with elements, $H_{ij} = \langle \phi_i|\hat{H}_P(R)|\phi_j\rangle$, and S is the overlap matrix with elements, $S_{ij} = \langle \phi_i|\phi_j\rangle$. The matrix elements $\{H_{ij}\}$ and $\{S_{ij}\}$ were evaluated numerically using the trapezoid rule for integration with 40 points evenly spaced over a region from $q=-1.5$ Å to $q=0.95$ Å. The coefficients $\{c_{i\alpha}\}$ satisfy the normalization condition, $\sum_{ij} c_{i\alpha} S_{ij} c_{j\alpha} = 1$.

The eigenvalue problem was solved at each molecular-dynamics (MD) time step to obtain $\{c_{i\alpha}\}$ and $\{|\alpha; R\rangle\}$. The ground-state Hellmann-Feynman forces, $-\langle 1; R|\nabla_R \hat{H}_P(R)|1; R\rangle$, were calculated using the numerical integration method described above. Given these Hellmann-Feynman forces, the classical equations of motion were integrated using the velocity Verlet algorithm and the RATTLE algorithm¹⁹ with a time step of 5 fs to yield a new classical configuration.

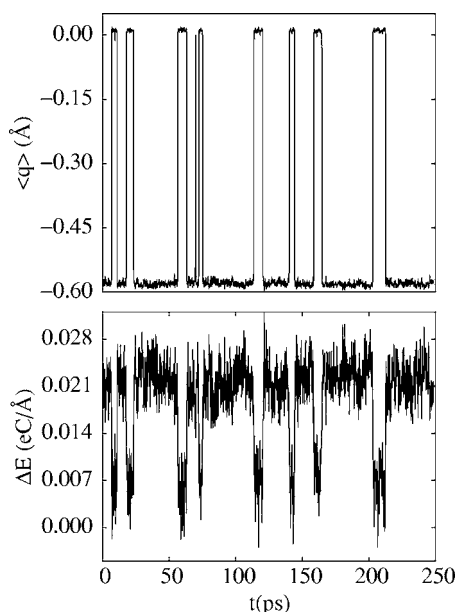


FIG. 1. Comparison of the time series of the mean position of the proton ($\langle q \rangle$) in the ground state and the solvent polarization (ΔE).

B. Reaction coordinate and free energy

The proton transfer dynamics was monitored by observing the evolution of the mean position of the proton in the ground adiabatic state, $\langle q \rangle(R) = \langle 1; R | \hat{q} | 1; R \rangle$, and the solvent polarization, $\Delta E(R)$,

$$\Delta E(R) = \sum_{i,a} z_a e \left(\frac{1}{|R_i^a - s|} - \frac{1}{|R_i^a - s'|} \right), \quad (5)$$

where $z_a e$ ($e = 1.602 \times 10^{-19}$ C) is the charge on atom a , and s and s' are two points within the complex, one at the center of mass and the other displaced by -0.56 Å from the center of mass, respectively, which correspond to the minima of the bare potential. The sums run over all solvent molecules i and atoms a . The solvent polarization is the difference between the solvent electrical potentials at points s and s' and probes the effects of solvent dynamics on the proton transfer reaction. Both of these reaction coordinates are functions of all of the positions of the classical particles.

In Fig. 1 we see that both the time series of $\langle q \rangle$ and ΔE track the hops of the proton between the reactant state ($\langle q \rangle \approx 0$ Å, $\Delta E \approx 0.005$ eC/Å) and the product state ($\langle q \rangle \approx -0.57$ Å, $\Delta E \approx 0.0225$ eC/Å). The complex spends more time in the ionic configuration than in the covalent configuration since electrostatic interactions with the polar solvent preferentially stabilize the ionic configuration of the complex. This should be contrasted with the situation in the gas phase, where the complex is primarily found in the covalent configuration.

The mechanism for the proton transfer can be inferred from the information in Fig. 2. From an examination of a sample proton hop, we see that an extensive, rapid solvent polarization takes place in 210 fs to induce a very rapid shift of the protonic charge in 35 fs (taking the complex from the ionic to the covalent configuration), followed by a rapid solvent rearrangement occurring in 105 fs in response to the

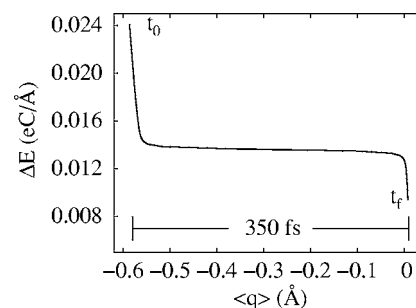


FIG. 2. Solvent polarization, ΔE , as a function of the mean position of the proton, $\langle q \rangle$, along a proton transfer event with $t_f - t_0 = 350$ fs, where t_f is the final time and t_0 is the initial time.

new protonic configuration. This shift in the protonic charge only occurs for a very narrow window of solvent polarization values. A similar correlation between ΔE and $\langle q \rangle$ was observed over the course of a long trajectory containing many proton hops, thereby confirming this mechanism.

Further insight into the adiabatic proton transfer mechanism can be obtained from the structure of the free energy along the reaction coordinate. Letting $\xi(R)$ denote a general reaction coordinate, the free energy is given by

$$\beta W(\xi') = -\ln \frac{P(\xi')}{P_u}, \quad (6)$$

where $\beta = 1/k_B T$, P_u is the uniform probability density of ξ , and

$$P(\xi') = \frac{\int dR dP \delta(\xi(R) - \xi') e^{-\beta H_1}}{\int dR dP e^{-\beta H_1}} \quad (7)$$

is the probability density for finding the numerical value ξ' of $\xi(R)$ with the proton confined to the ground-state 1 in adiabatic dynamics. The Hamiltonian $H_1 = \sum_i P_i^2 / (2M_i) + E_1(R)$, where the sum runs over all classical particles i , and P_i and M_i are the momentum and mass of the i th particle, respectively.

The probability $P(\xi')$ can be estimated directly by binning the results from a long canonical dynamics trajectory on the ground adiabatic surface and the free energy can then be computed from $\beta W(\xi') = -\ln \langle \delta(\xi(R) - \xi') \rangle$ where the angular brackets $\langle \dots \rangle$ are defined by

$$\langle \dots \rangle = \frac{\int dR dP \dots e^{-\beta H_1}}{\int dR dP e^{-\beta H_1}}. \quad (8)$$

Figures 3 and 4, respectively, show the ground-state free energies for $\xi = \langle q \rangle$ and $\xi = \Delta E$. In Fig. 3 we see that the barrier region is very broad making it difficult to locate the transition state region. The free energy along the ΔE coordinate shown in Fig. 4 has a different structure. There is a sharply defined barrier region and approximately harmonic stable wells. In order to estimate the activation free energy ($\Delta W(\Delta E^\ddagger)$), the wells of the ground-state free-energy surface

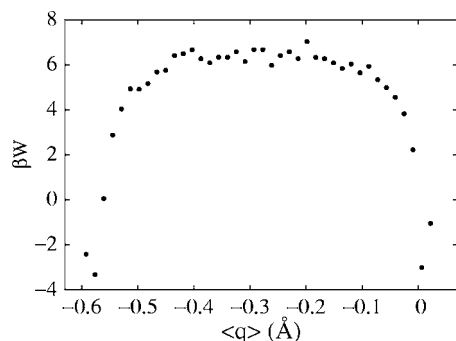


FIG. 3. Free-energy (βW) profile along the $\langle q \rangle$ coordinate for the ground-state dynamics.

were fitted with parabolas (shown in the figure) and a value of $\Delta W(\Delta E^\ddagger) = W(\Delta E^\ddagger) - W(\Delta E_{\min}) = 2.71 kT = 1.35 \text{ kcal mol}^{-1}$ was obtained for the forward rate process. Here, $\Delta E^\ddagger = 0.0141 eC/\text{\AA}$ and $\Delta E_{\min} = 0.0065 eC/\text{\AA}$ are the values of ΔE at the transition state and at the minimum of the covalent well, respectively. It is evident from the plot that the minimum of the (ionic) product state is lower in free energy than that of the (covalent) reactant state as a result of the stabilizing effect of the polar solvent. In accord with considerations by Kiefer and Hynes,²⁰ these features make ΔE a preferable reaction coordinate for the study of the proton transfer dynamics.

C. Time-dependent adiabatic rate coefficient

The rate of the proton transfer process was determined from the reactive-flux correlation function expression employing $\Delta E(R)$ as the reaction coordinate. The time-dependent reactive-flux correlation function²¹ is given by

$$k(t) = \frac{\langle \Delta \dot{E}(0) \theta(\Delta E(t) - \Delta E^\ddagger) \delta(\Delta E(0) - \Delta E^\ddagger) \rangle}{\langle \theta(\Delta E^\ddagger - \Delta E(t)) \rangle \langle \theta(\Delta E(t) - \Delta E^\ddagger) \rangle} \equiv \kappa(t) k^{\text{TST}}, \quad (9)$$

where $\theta(x)$ is the Heaviside function which selects the left or right species. The dividing surface $\Delta E = \Delta E^\ddagger$ separates reactants from products and the ensemble average needed to compute $k(t)$ is conditioned on the reaction coordinate being on this dividing surface. The second equality in Eq. (9) expresses $k(t)$ as the product of the transition state theory

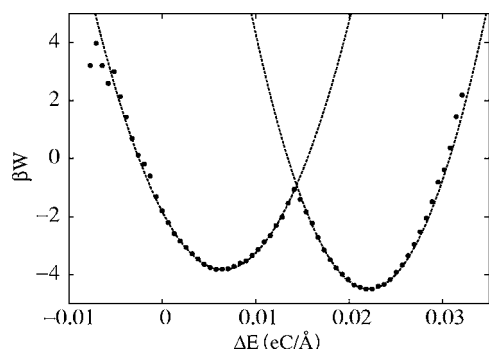


FIG. 4. Free-energy (βW) profile along the ΔE coordinate for the ground-state dynamics. The circles are the results obtained from a 2.5-ns trajectory. The lines are the quadratic fits to the free-energy minima.

(TST) rate constant and $\kappa(t)$, the time-dependent transmission coefficient which determines deviations from TST. The conditional average in the expression for $k(t)$ can be computed in terms of a “blue moon” ensemble²² where the reaction coordinate is fixed by a holonomic constraint at $\Delta E = \Delta E^\ddagger$. The expressions for $\kappa(t)$ and k^{TST} then take the forms,

$$\kappa(t) = \frac{\langle D^{-1/2} \Delta \dot{E}(0) \theta(\Delta E(t) - \Delta E^\ddagger) \rangle_{\Delta E^\ddagger}}{\langle D^{-1/2} \Delta \dot{E}(0) \theta(\Delta \dot{E}(0)) \rangle_{\Delta E^\ddagger}}, \quad (10)$$

and

$$k^{\text{TST}}(t) = (2\pi\beta)^{-1/2} \langle D^{-1/2} \rangle_{\Delta E^\ddagger}^{-1} \times \frac{\langle \delta(\Delta E - \Delta E^\ddagger) \rangle}{\langle \theta(\Delta E^\ddagger - \Delta E) \rangle \langle \theta(\Delta E - \Delta E^\ddagger) \rangle}, \quad (11)$$

where $\langle \dots \rangle_{\Delta E^\ddagger}$ denotes an average over an ensemble of trajectories with $\Delta E = \Delta E^\ddagger$ fixed by a holonomic constraint on the equations of motion. The factor $D^{-1/2}$ removes the bias introduced by the blue moon sampling and for our system is given by⁶

$$D = \frac{1}{M_S} \sum_i \left(\sum_a \frac{\partial \Delta E}{\partial R_{i,a}} \right)^2 + \frac{1}{M_C} \left(\sum_{\alpha=A,B} \frac{\partial \Delta E}{\partial R_\alpha} \right)^2, \quad (12)$$

where $M_S = m_{\text{CH}_3} + m_{\text{Cl}}$ and $M_C = m_A + m_B$ are the sums of the masses of the atoms comprising solvent molecules and the complex, respectively.

To determine the transmission coefficient, $\kappa(t)$, an ensemble of initial conditions was generated using blue moon sampling from a long constant temperature trajectory with $\Delta E = \Delta E^\ddagger$. At well-separated points along this trajectory the constraint was released and particle velocities were assigned according to the generalization of Boltzmann sampling for rigid diatomic molecules.²³ To compute k^{TST} , the quantity $\langle D^{-1/2} \rangle_{\Delta E^\ddagger}^{-1}$ was evaluated using blue moon sampling while the averages of any function $f(\Delta E(R))$, $\langle f(\Delta E(R)) \rangle$, were computed by numerical integration of the ground-state free energy,

$$\begin{aligned} \langle f(\Delta E(R)) \rangle &= \int d\Delta E' f(\Delta E') \langle \delta(\Delta E' - \Delta E(R)) \rangle \\ &= \int d\Delta E' f(\Delta E') e^{-\beta W(\Delta E')} P_u, \end{aligned} \quad (13)$$

where $P_u = (\int d\Delta E' e^{-\beta W(\Delta E')})^{-1}$.

In Fig. 5, we present results for the time-dependent adiabatic rate coefficient $k(t)$ which were obtained from an average over 16 000 trajectories. After a very sharp fall from its k^{TST} value in a few tenths of a picosecond, one observes a slower decay to a plateau, characteristic of the proton transfer process. To eliminate the slow decay of $k(t)$ to zero on the time scale of the proton transfer process, we introduced absorbing boundaries at the well minima of the free-energy potential. We confirmed that the rate constant determined from the plateau value with absorbing boundaries is the same, within statistical uncertainty, as that obtained from the extrapolation of the long-time decay of $k(t)$ determined with-

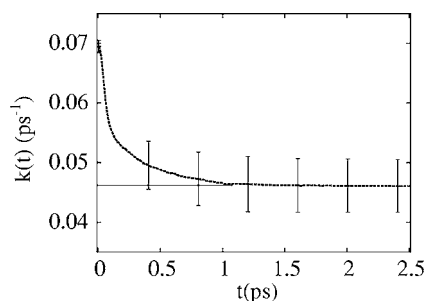


FIG. 5. Adiabatic rate coefficient as a function of time. The error bars represent ± 1 standard deviation.

out absorbing boundaries to its value at $t=0$. The value of k obtained from the plateau of $k(t)$ is $k=0.046 \text{ ps}^{-1}$.

The rate constant $k=k_f+k_r$, which is the sum of the forward and reverse rate constants, determines the overall chemical relaxation time, $\tau_{\text{chem}}=k^{-1}$, for the proton transfer. The individual forward and reverse rate constants, k_f and k_r , respectively, may be obtained by using the expression $K_{\text{eq}}=k_f/k_r$ for the equilibrium constant in conjunction with the known value of k . We find, $K_{\text{eq}}=1.74$, $k_f=0.027 \text{ ps}^{-1}$, and $k_r=0.019 \text{ ps}^{-1}$. The transmission coefficient was estimated to be $\kappa=0.66$, which indicates that there is a non-negligible deviation from k^{TST} for this proton transfer process.

IV. NONADIABATIC DYNAMICS

Coupling between the solvent motions and the quantum protonic degree of freedom can induce quantum transitions among the protonic adiabatic states. In this case the dynamics is no longer confined to the ground-state surface and a full nonadiabatic treatment of the reaction dynamics is necessary. In this section we show how the quantum-classical Liouville formulation¹⁸ of nonadiabatic dynamics can be used to compute the reaction rate.

The protonic excited-state structure can be analyzed by computing the free energy along the reaction coordinate for different protonic adiabatic energy surfaces, $\beta W_\alpha(\xi') = -\ln[P_\alpha(\xi')/P_u]$, where now

$$P_\alpha(\xi') = \frac{\int dR dP \delta(\xi(R) - \xi') e^{-\beta H_\alpha}}{\sum_\alpha \int dR dP e^{-\beta H_\alpha}}, \quad (14)$$

is the probability density for finding the numerical value ξ' of $\xi(R)$ with the proton in state α with $H_\alpha = \sum_i P_i^2 / (2m_i) + E_\alpha(R)$. We may write the free energy as

$$\beta W_\alpha(\xi') = -\ln \frac{\langle \delta(\xi(R) - \xi') \rangle_\alpha}{P_u} - \ln \frac{p_\alpha}{p_1}, \quad (15)$$

where the angular brackets $\langle \cdots \rangle_\alpha$ are defined by

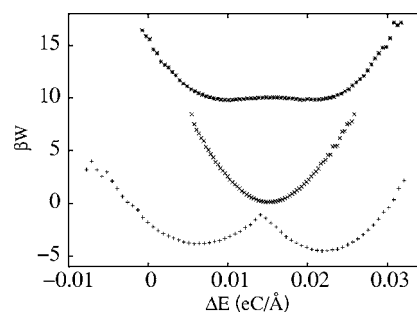


FIG. 6. Free-energy (βW) profiles along the ΔE coordinate for the ground, first, and second excited-state dynamics.

$$\langle \cdots \rangle_\alpha = \frac{\int dR dP \cdots e^{-\beta H_\alpha}}{\int dR dP e^{-\beta H_\alpha}}. \quad (16)$$

The probability that the system is in state α is $p_\alpha = \int d\xi' P_\alpha(\xi')$, and therefore

$$\frac{p_\alpha}{p_1} = \frac{\int dR dP e^{-\beta(E_\alpha - E_1)} e^{-\beta H_1}}{\int dR dP e^{-\beta H_1}}. \quad (17)$$

The free-energy profiles, constructed by binning the results of long (2.5 ns) adiabatic dynamics trajectories on the ground, first, and second excited-state surfaces, are shown in Fig. 6. We have chosen to fix the additive constant so that the free-energy curves are displaced by the logarithm of the factor in Eq. (17) from the ground-state curve. This factor is related to the relative probability that the system is in state α (regardless of the value of $\xi=\Delta E$), and can be determined from a long adiabatic trajectory on the ground-state surface. The free energy in the first excited state has a single-well structure, in contrast with the double-well ground state, with a minimum displaced to the ionic proton-ion complex configuration due to coupling with the second excited state. The second excited-state free energy has a double-well structure with a relatively low barrier. Given the magnitude of the energy gap between the first and second excited-state surfaces, only the ground and first excited states are expected to participate strongly in the nonadiabatic dynamics. It is worth stressing that the nonadiabatic dynamics calculations we carry out here are *not* based on these free-energy profiles but instead involve dynamics on the actual adiabatic energy surfaces or on averages of adiabatic energy surfaces.

A. Time-dependent nonadiabatic rate coefficient

The quantum-classical Liouville expression for the time-dependent rate coefficient, $k_{AB}(t)=k_r(t)^{24}$ is

$$k_{AB}(t) = -(\beta n_A^{\text{eq}})^{-1} \sum_{\alpha\alpha'} \int dR dP N_B^{\alpha\alpha'}(t) (\hat{N}_A, \hat{p} W_e)_{\alpha\alpha'}, \quad (18)$$

where the quantum-classical bracket is defined by $(\hat{A}, \hat{B}) = \frac{i}{\hbar} [\hat{A}, \hat{B}] - \frac{1}{2} (\{\hat{A}, \hat{B}\} - \{\hat{B}, \hat{A}\})$ and $\{\cdot, \cdot\}$ is the Poisson bracket.

The solvent polarization will again be used to track the reaction dynamics so we select A and B species variables as, $\hat{N}_A = \theta(\Delta E(R) - \Delta E^\ddagger) \equiv \Theta_A$ and $\hat{N}_B = \theta(\Delta E^\ddagger - \Delta E(R)) \equiv \Theta_B$, with $n_A^{\text{eq}} = \int d\Delta E' \Theta_A e^{-\beta W(\Delta E')} P_u$. In this case the quantum-classical bracket in Eq. (18) takes the following form in the adiabatic basis:

$$(\hat{N}_A, \hat{\rho}_{W_e})_{\alpha\alpha'} = -\{\Theta_A, \hat{\rho}_{W_e}^{\alpha\alpha'}\} = -\frac{\partial \Theta_A}{\partial R} \cdot \frac{\partial \rho_{W_e}^{\alpha\alpha'}}{\partial P}. \quad (19)$$

The equilibrium canonical density matrix $\rho_{W_e}^{\alpha\alpha'}$ is stationary under quantum-classical evolution but its explicit form is not known in general. However, it is known to first order in the smallness parameter $\mu = (m/M)^{1/2}$ (when scaled variables are used) and to this order it coincides with the exact quantum canonical density matrix. (An upper bound on μ is given by $\mu_{\text{max}} = (m_P/m_{\text{CH}_3})^{1/2} \approx 0.4$.) To this order $\rho_{W_e}^{\alpha\alpha'}$ is given by²⁵

$$\rho_{W_e}^{\alpha\alpha'} = \rho_{W_e}^{(0)\alpha} \delta_{\alpha\alpha'} - i\hbar f_{W_e}^{\alpha\alpha'} (1 - \delta_{\alpha\alpha'}), \quad (20)$$

where

$$\rho_{W_e}^{(0)\alpha} = Z_0^{-1} e^{-\beta H_W^\alpha}, \quad Z_0 = \sum_\alpha \int dR dP e^{-\beta H_W^\alpha}, \quad (21)$$

and

$$f_{W_e}^{\alpha\alpha'} = \frac{P}{M} \cdot d_{\alpha\alpha'} \rho_{W_e}^{(0)\alpha} \left(\frac{\beta}{2} (1 + e^{-\beta E_{\alpha'\alpha}}) + \frac{1 - e^{-\beta E_{\alpha'\alpha}}}{E_{\alpha\alpha'}} \right). \quad (22)$$

Using these results, the time-dependent rate coefficient can be decomposed into the sum of two contributions:

$$k_{AB}(t) = k_{AB}^d(t) + k_{AB}^o(t). \quad (23)$$

The diagonal part of the density matrix gives rise to the contribution

$$k_{AB}^d(t) = (\beta n_A^{\text{eq}})^{-1} \sum_\alpha \int dR dP N_B^{\alpha\alpha}(R, P, t) \times \frac{\partial \Theta_A}{\partial R} \cdot \frac{\partial \rho_{W_e}^{\alpha\alpha}}{\partial P}. \quad (24)$$

The off-diagonal part of the density matrix yields

$$k_{AB}^o(t) = -\frac{2\hbar}{\beta n_A^{\text{eq}}} \sum_{\alpha < \alpha'} \int dR dP \text{Im}\{N_B^{\alpha\alpha'}(R, P, t)\} \times \frac{\partial \Theta_A}{\partial R} \cdot \frac{\partial f_{W_e}^{\alpha\alpha'}}{\partial P}. \quad (25)$$

After performing the derivatives in Eq. (24) we find that the diagonal contribution is

$$k_{AB}^d(t) = -\frac{1}{n_A^{\text{eq}}} \sum_\alpha \int dR dP \Delta \dot{E}(R) N_B^{\alpha\alpha}(R, P, t) \times \delta(\Delta E(R) - \Delta E^\ddagger) \rho_{W_e}^{\alpha\alpha}, \quad (26)$$

where $\Delta \dot{E}(R) = P/M \cdot \nabla_R \Delta E(R)$. This is the major contribution to the rate coefficient. We have found that the off-

diagonal term yields a negligible contribution to the rate coefficient for the model under study and hence will not be further considered. Equation (26) provides a well-defined formula involving sampling from the barrier top and can be used to calculate the time-dependent rate coefficient $k_{AB}(t)$. In addition to sampling from the barrier top, quantum-classical time evolution of $N_B^{\alpha\alpha'}(R, P, t)$ must be carried out to determine the reaction rate.

B. Evolution of the species operator

The quantum-classical Liouville equation for the chemical species operator $\hat{N}_B(R, P, t)$ is¹⁸

$$\begin{aligned} \frac{d}{dt} \hat{N}_B(R, P, t) &= \frac{i}{\hbar} [\hat{H}, \hat{N}_B(t)] - \frac{1}{2} (\{\hat{H}, \hat{N}_B(t)\} - \{\hat{N}_B(t), \hat{H}\}) \\ &= i\hat{\mathcal{L}} \hat{N}_B(R, P, t). \end{aligned} \quad (27)$$

The formal solution of this equation is easily written as $\hat{N}_B(t) = \exp(i\hat{\mathcal{L}}t) \hat{N}_B(0)$.

We use the sequential short-time propagation scheme²⁶ to simulate the quantum-classical evolution. The propagator, $\exp(i\hat{\mathcal{L}}t)$, can be decomposed into a composition of propagators in time segments of arbitrary length. The evolution of a dynamical variable over any time interval can then be obtained by the successive application of evolution operators in the small time segments.

In the adiabatic basis, $\hat{\mathcal{L}}$ has matrix elements¹⁸

$$\begin{aligned} i\mathcal{L}_{\alpha\alpha', \beta\beta'} &= (i\omega_{\alpha\alpha'} + iL_{\alpha\alpha'}) \delta_{\alpha\beta} \delta_{\alpha'\beta'} - J_{\alpha\alpha', \beta\beta'} \\ &\equiv i\mathcal{L}_{\alpha\alpha'}^0 \delta_{\alpha\beta} \delta_{\alpha'\beta'} - J_{\alpha\alpha', \beta\beta'}, \end{aligned} \quad (28)$$

where the frequency $\omega_{\alpha\alpha'}(R) = (E_\alpha(R) - E_{\alpha'}(R))/\hbar$ and the classical Liouville operator $L_{\alpha\alpha'}$ is

$$iL_{\alpha\alpha'} = \frac{P}{M} \cdot \frac{\partial}{\partial R} + \frac{1}{2} (F_W^\alpha + F_W^{\alpha'}) \cdot \frac{\partial}{\partial P}. \quad (29)$$

Here F_W^α is the Hellmann–Feynman force that governs the motion on the adiabatic surface corresponding to state α . The term $J_{\alpha\alpha', \beta\beta'}$ is responsible for the momentum transfer to and from the bath that accompanies nonadiabatic transitions and has the form

$$\begin{aligned} J_{\alpha\alpha', \beta\beta'} &= -\frac{P}{M} \cdot d_{\alpha\beta} \left(1 + \frac{1}{2} S_{\alpha\beta} \cdot \frac{\partial}{\partial P} \right) \delta_{\alpha'\beta'} - \frac{P}{M} \cdot d_{\alpha'\beta'}^* \\ &\quad \times \left(1 + \frac{1}{2} S_{\alpha'\beta'}^* \cdot \frac{\partial}{\partial P} \right) \delta_{\alpha\beta}, \end{aligned} \quad (30)$$

where $S_{\alpha\beta} = (E_\alpha - E_\beta) d_{\alpha\beta} (P/M \cdot d_{\alpha\beta})^{-1}$ and the nonadiabatic coupling matrix element $d_{\alpha\beta} = \langle \alpha; R | \partial / \partial R | \beta; R \rangle$.

In the adiabatic basis $N_B^{\alpha\alpha'}(R, P, t)$ is given by

$$N_B^{\alpha\alpha'}(R, P, t) = \sum_{\alpha_N \alpha'_N} (e^{i\hat{\mathcal{L}}t})_{\alpha\alpha', \alpha_N \alpha'_N} N_B^{\alpha_N \alpha'_N}(R, P). \quad (31)$$

Consider dividing the time interval t into N segments such that the j th segment has length $\Delta t_j = t_j - t_{j-1} = \Delta t$ (which may be chosen to either equal or be an integer multiple of the time step of the simulation). We may then write

$$(e^{i\hat{L}t})_{\alpha_0\alpha'_0,\alpha_N\alpha'_N} = \sum_{(\alpha_1\alpha'_1)\dots(\alpha_{N-1}\alpha'_{N-1})} \prod_{j=1}^N (e^{i\hat{L}(t_j-t_{j-1})})_{\alpha_{j-1}\alpha'_{j-1},\alpha_j\alpha'_j}, \quad (32)$$

where $(\alpha_0\alpha'_0) \equiv (\alpha\alpha')$. If the time interval Δt is assumed to be sufficiently small, then we can approximate the quantum-classical propagator in an interval by

$$\begin{aligned} & (e^{iL(t_j-t_{j-1})})_{\alpha_{j-1}\alpha'_{j-1},\alpha_j\alpha'_j} \\ & \approx e^{iL_{\alpha_{j-1}\alpha'_{j-1}}(t_j-t_{j-1})} \\ & \quad \times (\delta_{\alpha_j\alpha'_j,\alpha_{j-1}\alpha'_{j-1}} - \Delta t J_{\alpha_{j-1}\alpha'_{j-1},\alpha_j\alpha'_j}) \\ & = \mathcal{W}_{\alpha_{j-1}\alpha'_{j-1}}(t_{j-1},t_j) e^{iL_{\alpha_{j-1}\alpha'_{j-1}}(t_j-t_{j-1})} \\ & \quad \times (\delta_{\alpha_j\alpha'_j,\alpha_{j-1}\alpha'_{j-1}} - \Delta t J_{\alpha_{j-1}\alpha'_{j-1},\alpha_j\alpha'_j}), \end{aligned} \quad (33)$$

where $\mathcal{W}_{\alpha_{j-1}\alpha'_{j-1}}(t_{j-1},t_j) = e^{i\omega_{\alpha_{j-1}\alpha'_{j-1}}(t_j-t_{j-1})}$ is the phase factor associated with that time segment. At the end of each time segment, the system either may remain in the same pair of adiabatic states or make a transition to a new pair of states.

Thus, the time evolution of the observable $N^{\alpha\alpha'}(R,P,t)$ can be calculated from

$$\begin{aligned} N_B^{\alpha\alpha'}(R,P,t) = & \sum_{(\alpha_1\alpha'_1)\dots(\alpha_N\alpha'_N)} \left[\prod_{j=1}^N (e^{i\hat{L}(t_j-t_{j-1})})_{\alpha_{j-1}\alpha'_{j-1},\alpha_j\alpha'_j} \right] \\ & \times N_B^{\alpha_N\alpha'_N}(R,P), \end{aligned} \quad (34)$$

where $\hat{N}_B^{\alpha\alpha'}(R,P) = \Theta_B \delta_{\alpha\alpha'}$. The multidimensional sums over quantum indices may be evaluated via Monte Carlo sampling while initial configurations may be sampled from $\rho_{W_e}^{11}$.

In the simulations of quantum-classical evolution using this algorithm, we used the momentum-jump approximation to compute the action of \hat{J} on phase-space functions. We use the fact that $\frac{1}{2}S_{\alpha\beta} \cdot \partial / \partial P = \Delta E_{\alpha\beta} \partial / \partial (\bar{P} \cdot \bar{d}_{\alpha\beta})^2$ where $\Delta E_{\alpha\beta} = E_\alpha - E_\beta$, $\bar{P} = P / \sqrt{M}$, and $\bar{d}_{\alpha\beta} = \hat{d}_{\alpha\beta} / \sqrt{M}$. Here we used the notation $\hat{d}_{\alpha\beta} / \sqrt{M} = \hat{d}_{\alpha\beta}^T M^{-1/2}$ and $\bar{P} \cdot \bar{d}_{\alpha\beta} = \bar{P}^T \hat{d}_{\alpha\beta} = \sum_j \bar{P}_j \hat{d}_{\alpha\beta}^j$ where T stands for the transpose, $M^{-1/2}$ is a diagonal matrix of the inverse square root masses, and the sum on j runs over all coordinates.

Using this notation the momentum-jump approximation is

$$\begin{aligned} \left(1 + \Delta E_{\alpha\beta} \frac{\partial}{\partial (\bar{P} \cdot \bar{d}_{\alpha\beta})^2} \right) f(P) & \approx e^{\Delta E_{\alpha\beta} \partial / \partial (\bar{P} \cdot \bar{d}_{\alpha\beta})^2} f(P) \quad (35) \\ & = f(P + \Delta P), \end{aligned}$$

where

$$\begin{aligned} \Delta P = & \sqrt{M} \bar{d}_{\alpha\beta} [\text{sgn}(\bar{P} \cdot \bar{d}_{\alpha\beta}) \sqrt{(\bar{P} \cdot \bar{d}_{\alpha\beta})^2 + \Delta E_{\alpha\beta}} \\ & - (\bar{P} \cdot \bar{d}_{\alpha\beta})]. \end{aligned} \quad (36)$$

From this equation we see that if $\Delta E_{\alpha\beta} < 0$ (an upward transition from $\alpha \rightarrow \beta$) and $(\bar{P} \cdot \bar{d}_{\alpha\beta})^2 < |\Delta E_{\alpha\beta}|$ so that there is

insufficient kinetic energy from bath momenta along $\bar{d}_{\alpha\beta}$ for the quantum transition to occur, the argument of the square root is negative leading to imaginary momentum changes. In this case, the quantum transition does not occur and the trajectory is continued adiabatically.

The total energy of the system is conserved along a quantum-classical surface-hopping trajectory when the momentum-jump approximation is used, even if the transition is to a pair of coherently coupled surfaces. This can be easily shown by comparing the total energy before and after a transition, using the form for the momentum shift given in Eq. (36).

C. Simulation algorithm

The nonadiabatic reactive-flux correlation function in Eq. (26) was evaluated using blue moon sampling as described in Sec. III for adiabatic dynamics. Only the form of the observable and the nature of the dynamics differ.

In order to illustrate the algorithm, it is instructive to calculate the evolution of the species variable $N_B^{\alpha_0\alpha'_0}(R,P,t)$ through two time segments. Given an initial configuration with $\Delta E(R) = \Delta E^\ddagger$ the value of $N_B^{\alpha_0\alpha'_0}(R,P,\Delta t)$ from Eq. (34),

$$\begin{aligned} N_B^{\alpha_0\alpha'_0}(R,P,\Delta t) = & \sum_{(\alpha_1\alpha'_1)} \mathcal{W}_{\alpha_0\alpha'_0}(\Delta t) e^{iL_{\alpha_0\alpha'_0}(t_1-t_0)} (\delta_{\alpha_1\alpha'_1,\alpha_0\alpha'_0} \\ & - \Delta t J_{\alpha_0\alpha'_0,\alpha_1\alpha'_1}) N_B^{\alpha_1\alpha'_1}(R,P) \\ = & \sum_{(\alpha_1\alpha'_1)} \mathcal{W}_{\alpha_0\alpha'_0}(\Delta t) (\delta_{\alpha_1\alpha'_1,\alpha_0\alpha'_0}(R_{\Delta t},P_{\Delta t}) \\ & - \Delta t J_{\alpha_0\alpha'_0,\alpha_1\alpha'_1}(R_{\Delta t},P_{\Delta t})) \\ & \times N_B^{\alpha_1\alpha'_1}(R_{\Delta t},P_{\Delta t}), \end{aligned} \quad (37)$$

is computed as follows: given $(\alpha_0\alpha'_0)$, the system phase point (R,P) is evolved by Δt to $(R_{\Delta t},P_{\Delta t})$ by using the classical propagator $e^{iL_{\alpha_0\alpha'_0}\Delta t}$. The phase factor $\mathcal{W}_{\alpha_0\alpha'_0}$ is then computed. We then choose with probability 1/2 whether the transition $\alpha_0 \rightarrow \alpha_1$ or $\alpha'_0 \rightarrow \alpha'_1$ occurs, corresponding to the two terms in $J_{\alpha_0\alpha'_0,\alpha_1\alpha'_1}$. We choose α_1 and α'_1 uniformly from the set of allowed final states. Therefore, the weight $w_{\alpha_0\alpha'_0,\alpha_1\alpha'_1}$ associated with the final state is the number of allowed final states. Having chosen $(\alpha_1\alpha'_1)$ [or $(\alpha_0\alpha'_0)$] we numerically calculate $d_{\alpha_0\alpha_1}$ (or $d_{\alpha'_0\alpha'_1}$) at the updated position $R_{\Delta t}$ by

$$d_{\alpha_0\alpha_1}(R_{\Delta t}) = - \frac{\langle \alpha_0; R_{\Delta t} | \nabla_{R_{\Delta t}} \hat{H}_P(R_{\Delta t}) | \alpha_1; R_{\Delta t} \rangle}{\Delta E_{\alpha_0\alpha_1}(R_{\Delta t})}. \quad (38)$$

We define the probability, Π , of a nonadiabatic transition as

$$\Pi = \left| \frac{P_{\Delta t}}{M} \cdot d_{\alpha_0\alpha_1}(R_{\Delta t}) \right| \Delta t \left(1 + \left| \frac{P_{\Delta t}}{M} \cdot d_{\alpha_0\alpha_1}(R_{\Delta t}) \right| \Delta t \right)^{-1}, \quad (39)$$

and sample with it:

(a) If the transition is rejected, then

$$N_B^{\alpha_0\alpha'_0}(R, P, \Delta t) = \mathcal{W}_{\alpha_0\alpha'_0}(\Delta t) N_B^{\alpha_0\alpha'_0}(R_{\Delta t}, P_{\Delta t}) \frac{1}{1 - \Pi}. \quad (40)$$

(b) If the transition is accepted, then, using the momentum-jump approximation, we translate the momentum $P_{\Delta t}$ to $\tilde{P}_{\Delta t} = P_{\Delta t} + \Delta P$ where ΔP is defined in Eq. (36). We then write

$$N_B^{\alpha_0\alpha'_0}(R, P, \Delta t) = \mathcal{W}_{\alpha_0\alpha'_0}(\Delta t) N_B^{\alpha_1\alpha'_0}(R_{\Delta t}, \tilde{P}_{\Delta t}) \times \Delta t \frac{P_{\Delta t}}{M} \cdot d_{\alpha_0\alpha_1}(R_{\Delta t}) \frac{1}{\Pi} w_{\alpha_0\alpha'_0, \alpha_1\alpha'_1}. \quad (41)$$

In order to proceed through the next time slice, we need to examine Eq. (34) with $N=2$ and consider the action of the leftmost exponential operator on the terms to the right of it:

$$\begin{aligned} N_B^{\alpha\alpha'}(R, P, 2\Delta t) &= \sum_{(\alpha_1\alpha'_1), (\alpha_2\alpha'_2)} \mathcal{W}_{\alpha_0\alpha'_0}(\Delta t) e^{iL_{\alpha_0\alpha'_0}(t_1-t_0)} (\delta_{\alpha_1\alpha'_1, \alpha_0\alpha'_0} - \Delta t J_{\alpha_0\alpha'_0, \alpha_1\alpha'_1}) (e^{i\hat{L}(t_2-t_1)})_{\alpha_1\alpha'_1, \alpha_2\alpha'_2} N_B^{\alpha_2\alpha'_2}(R, P) \\ &= \sum_{(\alpha_1\alpha'_1), (\alpha_2\alpha'_2)} \mathcal{W}_{\alpha_0\alpha'_0}(\Delta t) [\delta_{\alpha_1\alpha'_1, \alpha_0\alpha'_0}(R_{\Delta t}, P_{\Delta t}) - \Delta t J_{\alpha_0\alpha'_0, \alpha_1\alpha'_1}(R_{\Delta t}, P_{\Delta t})] e^{i\hat{L}_{\alpha_1\alpha'_1}(R_{\Delta t}, P_{\Delta t})(t_2-t_1)} (\delta_{\alpha_2\alpha'_2, \alpha_1\alpha'_1}(R_{\Delta t}, P_{\Delta t}) \\ &\quad - \Delta t J_{\alpha_1\alpha'_1, \alpha_2\alpha'_2}(R_{\Delta t}, P_{\Delta t})) N_B^{\alpha_2\alpha'_2}(R_{\Delta t}, P_{\Delta t}). \end{aligned} \quad (42)$$

The choice of the operators in the square brackets in the second equality of Eq. (42) yields either Eq. (40) or Eq. (41) of the first time slice. The calculation of $N_B^{\alpha_0\alpha'_0}(R, P, 2\Delta t)$ is then performed as outlined above for the first time slice, using the remaining operators in Eq. (42). This procedure is repeated to obtain $N_B^{\alpha_0\alpha'_0}(R, P, j\Delta t)$ for the j th time slice until the N th time slice is reached. Finally, averaging the resulting quantities over the initial conditions, we obtain the nonadiabatic time-dependent rate coefficient.

In practice, we set a bound n_{\max} on the maximum number of allowed nonadiabatic transitions in a trajectory so that at a time $t' \leq t$ when $n = n_{\max} + 1$, there is no contribution to the observable, i.e., the contribution to average in the time-dependent rate coefficient is zero, but the normalization factor is incremented. Because of this restriction, the calculation of $k_{AB}(t)$ will be accurate only for times for which the dynamics is accurately represented by $n \leq n_{\max}$ transitions (i.e., for times $t' \leq t$). This is termed the n_{\max} -jump contribution to the rate coefficient. Since $k_{AB}(t)$ involves trajectories starting at the barrier top and only short-time trajectories are needed to compute the rate, this is not a serious restriction. This restriction is imposed in order to avoid unnecessary accumulation of weight factors after convergence of the rate coefficient has been attained. In addition, we placed bounds on the observable such that if the bounds are exceeded, the value of the observable is set equal to the bound value. The purpose of these bounds is to prevent the excessive accumulation of weight factors, which can spoil the results. Within the regime that the bound is effective (i.e., regime in which the product of the weight factors is not excessively large), the bound value should be increased until the value of the observable has converged within statistical uncertainty. Since the bound has the effect of suppressing nonadiabatic effects, the value of the observable obtained is an upper bound on the true

value. On simple model reactive systems for which the rate may be determined without use of this approximation, we have confirmed that it yields the true value of the rate coefficient within statistical uncertainty. Since these restrictions are only imposed in the calculation of the reactive flux-correlation function, the nonadiabatic stochastic trajectories may be continued for long times without difficulty if needed.

In summary, while the simulation scheme for the rate constant outlined above involves an ensemble of surface-hopping trajectories, it differs from more traditional surface-hopping methods in a number of important respects. In such methods,^{2,7} the classical bath variables evolve on single adiabatic potential-energy surfaces according to Newton's equations of motion. Transitions between such surfaces are carried out stochastically with probabilities constructed to satisfy detailed balance. The reaction rate is computed by counting reactive events in small ensembles of long trajectories that pass from reactants to products several times.

As described above, in the present method, the rate constant is determined directly from the reactive-flux correlation function, which was derived from a linear-response analysis of the quantum-classical Liouville equation. The correlation function is simulated by a hybrid Monte Carlo–molecular-dynamics scheme where quantum transitions are sampled stochastically with probabilities determined from the coupling terms that appear in the quantum-classical propagation. The bias introduced in the sampling is accounted for by weight factors that appear in the expression for the correlation function.

The evolution of the species variable which appears in the reactive-flux correlation function is specified by the quantum-classical Liouville equation (27). This equation can be simulated in terms of an ensemble of surface-hopping trajectories. The nature of these surface-hopping trajectories has a character that differs from that in standard surface-

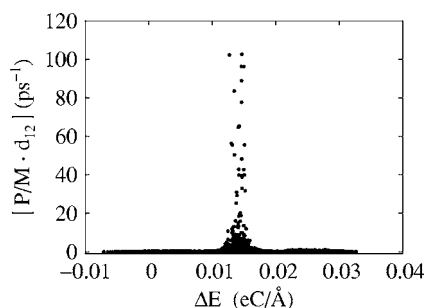


FIG. 7. $|P/M \cdot d_{12}|$ as a function ΔE for a long ground-state adiabatic trajectory.

hopping schemes. Each realization of the nonadiabatic dynamics is a single stochastic trajectory which involves classical evolution segments interspersed with quantum transitions that change one of the quantum states in the pair of states and produce momentum changes in the bath. In contrast with standard schemes, if the states in the pair are the same, then the classical evolution occurs on a single adiabatic potential-energy surface; however, if they are different, the evolution occurs on the mean of the two adiabatic surfaces. When evolution occurs on this mean surface, a phase factor is introduced to account for the coherent coupling between the two surfaces. Once the stochastic trajectories are computed, one may collect all the information needed to calculate the value of a species variable at all intermediate times and the reactive-flux correlation function.

D. Results

We now examine the effects of nonadiabatic transitions on the dynamics of this system. To obtain insight into the nature of the nonadiabatic dynamics, Fig. 7 shows $|P/M \cdot d_{12}|$ vs ΔE , which determines the probability of jumping between the ground and first excited adiabatic states. These results were obtained from a long adiabatic trajectory on the ground-state surface. One can see that this function is only high in a narrow region around the barrier top where the energy gap is small, so that the probability of a nonadiabatic transition is highest in this region.

Figure 8 (lower panel) shows the evolution of the solvent polarization $\Delta E(t)$ in a long nonadiabatic trajectory. The upper panel of the figure shows the protonic state along this trajectory. We use the coding $(1,1)=2$, $(1,2)=(2,1)=3$, and $(2,2)=4$. Nonadiabatic transitions only occur when $\Delta E(t)$ is in the vicinity of the barrier top and are associated with excursions in $\Delta E(t)$ across the barrier top. Not all reactive events as monitored by $\Delta E(t)$ are associated with nonadiabatic transitions, as can be seen from an examination of the figure. In addition, some of the crossings of the dividing surface which are associated with nonadiabatic transitions are immediately followed by recrossings. (See Fig. 9.) These failed proton transfer events will lead to a smaller transmission coefficient and thereby reduce the rate constant. When the system makes a transition to the “coherent” state $(1,2)$ or excited-state $(2,2)$ surface, it does not remain there long (tenths to a few picoseconds), but returns to the $(1,1)$ ground-state surface where it spends the majority of its time. As seen

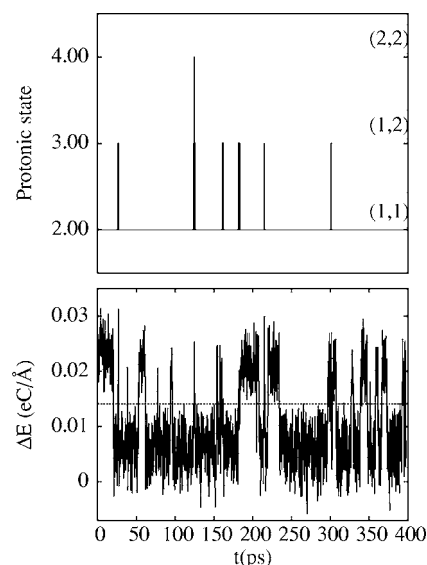


FIG. 8. A sample stochastic nonadiabatic trajectory. (Top) Protonic state as a function of time. (Bottom) ΔE as a function of time. The dotted line indicates the position of the barrier top.

in Fig. 8, transitions from the ground to the coherent-state surface and back are more frequent than transitions to the first excited-state surface and back. This indicates that transitions to the coherent-state surface will play a crucial role in this rate process.

We now turn to the calculation of $k_{AB}(t)$ from which the proton transfer rate constant can be estimated. Given that nonadiabatic transitions predominantly occur only in the vicinity of the barrier top, in our simulations of the reactive-flux correlation function we have used the window $0.0125 \text{ eC}/\text{\AA} \leq \Delta E \leq 0.016 \text{ eC}/\text{\AA}$, around the barrier top $\Delta E^\ddagger = 0.0141 \text{ eC}/\text{\AA}$, within which nonadiabatic transitions are allowed.

The “diagonal” term $k^d(t) = k_{AB}^d(t) + k_{BA}^d(t)$ [$k_{AB}^d(t)$ shown in Eq. (26)] has contributions arising from even numbers of

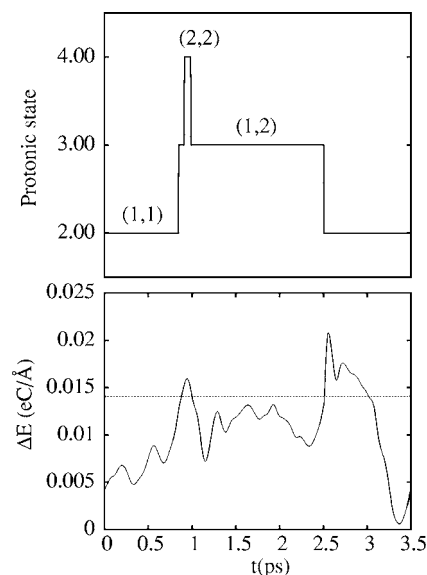


FIG. 9. A closer look at nonadiabatic transitions. (Top) Protonic state as a function of time. (Bottom) ΔE as a function of time. The dotted line indicates the position of the barrier top.

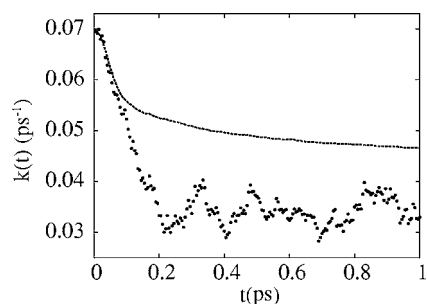


FIG. 10. Comparison between the nonadiabatic (points) and adiabatic (line) rate coefficients as a function of time.

nonadiabatic transitions. The contribution with no transitions is exactly the adiabatic result obtained earlier. The four-jump contribution [which was found to be sufficient for the convergence of $k^d(t)$] was obtained from an average over 16 000 trajectories. Since k_{AB}^o was found to be approximately zero, the overall nonadiabatic rate constant may be estimated by $k \approx k^d$. From the long-time decay of $k(t)$ shown in Fig. 10, a value of $k=0.035 \text{ ps}^{-1}$ was extracted. The contribution to k_d from the first excited state is not shown in the figure since it decays rapidly to zero and does not effect the plateau value. The transmission coefficient was estimated to be $\kappa \approx 0.48$.

Earlier studies of this model included vibration of the AB pair in the AHB complex. Since we have constrained the R_{AB} distance to illustrate the methodology in a simpler context, we cannot make quantitative comparisons of our numerical estimates of the reaction rate with those in earlier studies. Given the techniques developed in the paper, the more realistic case, where vibration of the AB complex is taken into account, can now be investigated using quantum-classical Liouville dynamics. Kinetic isotope effects can also be computed within this framework.

V. CONCLUSIONS

The calculations presented in this paper showed how reactive-flux expressions for nonadiabatic proton transfer processes could be simulated to obtain the proton transfer rate. Several aspects of the calculation are worth highlighting. The solvent polarization was found to be the most convenient reaction coordinate to monitor the proton transfer process in accord with earlier studies.²⁰ Apart from providing better insight into the mechanism of the transfer, since the solvent polarization depends only on the classical coordinates of the system, the rate formulas take a simple form that allows one to implement rare event sampling schemes to compute the reaction rate. Consequently, the formalism can be applied to highly activated rate processes that cannot be probed by simply following the dynamics over many reactive events. This is typically how the nonadiabatic rate constant is estimated using other surface-hopping schemes.^{11,15}

The picture of the nature of nonadiabatic effects is also different from that in standard surface-hopping schemes where transitions occur among adiabatic states and classical evolution takes place only on single adiabatic surfaces. In the quantum-classical Liouville approach, the members of the ensemble of trajectories that are used to estimate the rate execute classical evolution, either on single adiabatic sur-

faces or on the mean of two adiabatic surfaces of a coherently coupled pair of states. During the coherent evolution segments the expression for the observable contains a phase factor that reflects the quantum coherence. Thus, along a single nonadiabatic trajectory in the ensemble coherence is created and destroyed as a result of quantum transitions. We also note that the quantum-classical evolution operator ensures that energy is exactly conserved along a trajectory. If the momentum-jump approximation is used, energy is still exactly conserved along the nonadiabatic trajectories, preserving this important property.

When the mechanism of the nonadiabatic proton transfer rate was examined, we saw that the major nonadiabatic correction to the rate came from two quantum transitions. The first quantum transition takes the system to a coherent state (1,2) that couples the ground and first excited protonic states. The system evolves on the mean of these two adiabatic surfaces and the solvent polarization tends to remain longer near its transition state value. The second quantum transition takes the system back to the ground state and destroys the coherence created in the first transition. This leads to enhanced barrier recrossing and lowers the reaction rate. Contributions from four and higher numbers of quantum transitions and transitions to the excited state (2,2) occur but play a less important role. Thus, the mechanistic picture of how nonadiabatic effects influence the reaction is quite different from standard surface-hopping schemes.

It is difficult to simulate quantum-classical Liouville dynamics for long times and strong nonadiabaticity. The calculations of the rate constant presented here were possible because of the use of rare event sampling schemes that require only short-time dynamics. Further development of effective algorithms for simulating quantum-classical Liouville dynamics needs to be carried out to study a broader class of systems.

Finally, more realistic models of proton transfer should include vibration of the molecules in the proton complex. Incorporation of this feature does not present additional technical difficulties and future work will address this issue along with isotope effects on the transfer rate. The calculations reported above have served to illustrate the use of algorithms that were developed for computing nonadiabatic reaction rates in a simple model that incorporates many features of real systems. The techniques discussed here may be used for more realistic applications.

ACKNOWLEDGMENTS

This work was supported in part by a grant from the Natural Sciences and Engineering Research Council of Canada. One of the authors (G. H.) is grateful to A. Sergi for aid in starting this project and for many fruitful discussions.

¹R. P. Bell, *The Proton in Chemistry* (Chapman & Hall, London, 1973); *Electron and Ion Transfer in Condensed Media*, edited by A. A. Kornyshev, M. Tosi, and J. Ulstrup (World Scientific, Singapore, 1997).

²J. C. Tully, in *Modern Methods for Multidimensional Dynamics Computations in Chemistry*, edited by D. L. Thompson (World Scientific, New York, 1998), p. 34.

³M. F. Herman, *Annu. Rev. Phys. Chem.* **45**, 83 (1994).

- ⁴A. W. Jasper, C. Zhu, S. Nangia, and D. G. Truhlar, *Faraday Discuss.* **127**, 1 (2004).
- ⁵R. Kapral and G. Ciccotti, *Lect. Notes Phys.* **605**, 445 (2002).
- ⁶D. Laria, G. Ciccotti, M. Ferrario, and R. Kapral, *J. Chem. Phys.* **97**, 378 (1992).
- ⁷J. C. Tully, *J. Chem. Phys.* **93**, 1061 (1990); *Int. J. Quantum Chem.* **25**, 299 (1991).
- ⁸F. Webster, E. T. Wang, P. J. Rossky, and P. A. Friesner, *J. Chem. Phys.* **100**, 4835 (1994).
- ⁹D. F. Coker and L. Xiao, *J. Chem. Phys.* **102**, 496 (1995).
- ¹⁰H. Azzouz and D. C. Borgis, *J. Chem. Phys.* **98**, 7361 (1993).
- ¹¹S. Hammes-Schiffer and J. C. Tully, *J. Chem. Phys.* **101**, 4657 (1994).
- ¹²R. P. McRae, G. K. Schenter, B. C. Garrett, Z. Svetlicic, and D. G. Truhlar, *J. Chem. Phys.* **115**, 8460 (2001).
- ¹³D. Antoniou and S. D. Schwartz, *J. Chem. Phys.* **110**, 465 (1999).
- ¹⁴D. Antoniou and S. D. Schwartz, *J. Chem. Phys.* **110**, 7359 (1999).
- ¹⁵S. Y. Kim and S. Hammes-Schiffer, *J. Chem. Phys.* **119**, 4389 (2003).
- ¹⁶T. Yamamoto and W. H. Miller, *J. Chem. Phys.* **122**, 044106 (2005).
- ¹⁷J. P. Ryckaert, G. Ciccotti, and H. J. C. Berendsen, *J. Comput. Phys.* **23**, 327 (1977).
- ¹⁸R. Kapral and G. Ciccotti, *J. Chem. Phys.* **110**, 8919 (1999).
- ¹⁹H. C. Andersen, *J. Comput. Phys.* **52**, 24 (1983).
- ²⁰P. M. Kiefer and J. T. Hynes, *Solid State Ionics* **168**, 219 (2004).
- ²¹T. Yamamoto, *J. Chem. Phys.* **33**, 281 (1960).
- ²²E. Carter, G. Ciccotti, J. T. Hynes, and R. Kapral, *Chem. Phys. Lett.* **156**, 472 (1989).
- ²³G. Ciccotti and J. P. Ryckaert, *Comput. Phys. Rep.* **4**, 345 (1986).
- ²⁴A. Sergi and R. Kapral, *J. Chem. Phys.* **118**, 8566 (2003).
- ²⁵S. Nielsen, R. Kapral, and G. Ciccotti, *J. Chem. Phys.* **115**, 5805 (2001).
- ²⁶D. McKernan, R. Kapral, and G. Ciccotti, *J. Phys.: Condens. Matter* **14**, 9069 (2002).